Revised manuscript for: *Ultrasonics Sonochemistry*
Submission date: 2020-06-28

Enhanced Electrochemical Decontamination and Water Permeation of Titanium Suboxide Reactive Electrochemical Membrane Based on Sonoelectrochemistry

Jie Teng [a], Shijie You [a,*], Fang Ma [a], Xiaodong Chen [b], Nanqi Ren [a]

[a] *State Key Laboratory of Urban Water Resource and Environment, School of Environment, Harbin Institute of Technology, Harbin 150090, P. R. China.*
[b] *Innovative Centre for Flexible Devices (iFLEX), School of Materials Science and Engineering, Nanyang Technological University, 50 Nanyang Avenue, 639798, Singapore.*

Corresponding author:
P. O. Box 2603#, No. 73, Huanghe Road, Nangang District, Harbin, 150090, China.
Tel.: +86-451-86282008; Fax: +86-451-86282110
E-mail: sjyou@hit.edu.cn (SJ You)

Abstract

Reactive electrochemical membrane (REM) allows electrochemical oxidation (EO) water purification under flow-through operation, which improves mass transfer on the anode surface significantly. However, O_2 evolution reaction (OER) may cause oxygen bubbles to be trapped in small-sized confined flow channels, and thus degrade long-term filterability and treatability of REM. In this study, ultrasound (ultrasonic vibrator, 28 kHz, 180 W) was applied to EO system (i. e. sonoelectrochemistry) containing titanium suboxide-REM (TiSO-REM) anode for enhanced oxidation of 4-chlorophenol (4-CP) target pollutant. Both experimental and modeling results demonstrated that ultrasound could mitigate the retention of O_2 bubbles in the porous structures by destructing large-size bubbles, thus not only increasing permeate flux but also promoting local mass transfer. Meanwhile, oxidation rate of 4-CP for EO with ultrasound (EO-US, 0.0932 min^{-1}) was 216% higher than that for EO without ultrasound (0.0258 min^{-1}), due to enhanced mass transfer and •OH production under the cavitation effect of ultrasound. Density functional theory (DFT) calculations confirmed the most efficient pathway of 4-CP removal to be direct electron transfer of 4-CP to form $[4\text{-CP}]^{\bullet+}$, followed by subsequent oxidation mediated by •OH produced from anodic water oxidation on TiSO-REM anode. Last, the stability of TiSO-REM could be improved considerably by application of ultrasound, due to alleviation of electrode deactivation and fouling, indicated by cyclic test, scan electron microscopy (SEM) observation and Fourier transform infrared spectroscopy (FT-IR) characterization. This study provides a proof-of-concept demonstration of ultrasound for enhanced EO of recalcitrant organic pollutants by REM anode, making decentralized wastewater treatment more efficient and more reliable.

Keywords: Reactive electrochemical membrane; Oxygen evolution reaction; Sonoelectrochemistry; Ultrasound; 4-chlorophenol.

1. Introduction

Electrochemical oxidation (EO) has attracted an increasing attention as a promising technology for decentralized water and wastewater treatment by virtue of high efficiency, cleanliness and ease of automation. In EO process, recalcitrant organic pollutants can be decomposed via the mechanisms of direct electron transfer (DET) with anode (Eq. 1) and/or indirect oxidation mediated by reactive oxidative species (e. g. •OH, Cl_2, HClO, $SO_4^{\bullet-}$) (Eqs. 2 and 3) [1, 2]. Since organic pollutants are oxidized at a rate much faster than they migrate from bulk solution to anode surface, the overall EO performance is generally dominated by mass transfer process for flow-by operation. To alleviate this limitation, recent attention has been paid to reactive electrochemical membrane (REM), a newly developed anode material that works on flow-through operation during electrolysis [3]. The flow-through filtration operation allows REM to achieve a significantly enhanced mass transfer, which results in an EO rate being approximately several folds higher than that of traditional flow-by mode [3-5]. The highly porous structure of REM provides the anode material with a large specific surface area and more active sites for electrochemical reactions. This not only enhances electrochemical oxidation of pollutants, but also accelerates oxygen evolution reaction (OER, Eq. 4) [6, 7].

$$R \rightarrow (gR)^+ + e^- \quad (1)$$

$$H_2O \rightarrow gOH + H^+ + e^- \ (E^0 = 2.38 \text{ V vs SHE}) \quad (2)$$

$$gOH + R / (gR)^+ \rightarrow CO_2 + H_2O + H^+ + e^- \quad (3)$$

$$2H_2O \rightarrow O_2 + 4H^+ + 4e^- \ (E^0 = 1.23 \text{ V vs SHE, pH=0}) \quad (4)$$

In EO process, however, OER is an unwanted side reaction that may cause a decrease in overall current efficiency and an increase in energy consumption. Apart from these negative impacts, the

REM may have additional problems associated with OER because the adsorbed oxygen bubbles grow gradually in size followed by detachment from the anode surface under the action of buoyancy, surface tension, inertial force and shear force [8, 9], and eventually are trapped in the confined space of the microporous flow channels. The resulting large-sized oxygen bubbles, once formed, are unlikely to be removed easily, which may lead to performance decay during long-term operation by reducing effective volume accessible for liquid filtration, lowering current efficiency, blocking the active sites, and hindering contact between the pollutants and the anode surface [10]. Therefore, it will be highly desirable to develop effective strategies to mitigate negative impacts of OER for REM to increase overall efficiency of EO process for water purification.

Ultrasound irradiation has been accepted as a useful approach to eliminating gas bubbles from molten metals and alloys in metallurgy industry [11-15]. In the ultrasonic degassing process, propagation of high-frequency (>16 kHz) pressure waves in a fluid can result in periodical compression and rarefaction of the medium, during which cavitation effect initiates the collapse of gas bubbles within just a few microseconds [16-18]. Therefore, we expect that ultrasound may find its application for oxygen removal in REM-based EO process to enhance membrane permeate flux and pollutants abatement [19, 20]. In reality, combining electrochemistry with ultrasound gives rise to an interdisciplinary concept of sonoelectrochemistry [17, 21], which deals with electrochemical processes that are influenced, facilitated or enhanced by ultrasound. The synergistic sonoelectrochemical interaction offers the unique advantages of producing more •OH radicals assisted by cavitation effect, improving hydrodynamics and mass transfer, removing gas bubbles at the electrode surface, and inducing cleaning effect upon electrode surface [22-25]. These properties lead the sonoelectrochemistry to find several applications in the fields of water electrolysis for

hydrogen production, synthesis of electrocatalysts for fuel cells, as well as degradation of harmful substances for environmental remediation [26, 27]. To the best of our knowledge, however, there have been no report on applying sonoelectrochemistry to REM-based EO process.

Herein, we make an attempt to enhance EO decontamination and water permeation of titanium suboxide-REM (TiSO-REM) assisted by sonoelectrochemistry. The TiSO has conductivity approaching that of metal and excellent corrosion resistance that is close to that of ceramics. The unique advantages of high conductivity, good stability, high oxygen evolution potential, efficient mass transfer and low cost make TiSO-REM a promising anode material for electrochemical water purification [9, 28-31]. The 4-chlorophenol (4-CP) was selected specifically as the target organic pollutant because of its wide industrial applications, high eco-toxicity, and recalcitrant property [32-35].

The present study is organized as follows. First, we investigated the impact of oxygen bubbles produced from OER on filtration flux and visualized the role of ultrasound by using COMSOL Multiphysics. Second, the electrochemical degradation of 4-CP was studied and compared in the absence (EO) and presence (EO-US) of ultrasound. Third, the mechanisms for 4-CP degradation were underlined by performing electrochemical tests, electron spin resonance (ESR) spectroscopy, and density functional theory (DFT) calculations. Last, the long-term stability of EO system was assessed to interpret the function of ultrasound in mitigating electrode fouling.

2. Materials and methods

2.1. Chemicals and Electrode Material

All the chemicals were purchased from Sigma-Aldrich (China-mainland) or Macklin (Shanghai,

China) and used without any further purification. All the aqueous solutions were prepared by de-ionized water (DI-water) produced by PureLab Prima (ELGA LabWater, U.K.). The TiSO-REM anode (total length of 7.7 cm, inner and outer diameters of 2.3 and 2.8 cm) was supplied by Ti-Dynamics Co. Ltd, China. In brief, the rutile TiO_2 was reduced in H_2 atmosphere at 1593.15 K to form TiSO powder, which was then sintered with carbon as porosity-producing agent [31, 36, 37]. A flexible stainless steel (SS) mesh (7.5 cm×30 cm) served as the cathode.

2.2. Characterization

The crystalline phase of TiSO-REM was identified by X-ray diffraction (XRD, D8 ADVANCE, Bruker, Germany) by using monochromatized CuKα radiation (λ=0.15418 nm) at an accelerating voltage of 40 kV and a current of 40 mA. The composition and valence state of TiSO-REM were determined by X-ray photoelectron spectroscopy (XPS, ESCALAB 250 Xi, Al Kα radiation, Thermo Fisher Scientific, U.S.A.). The morphology and elemental composition of TiSO-REM were determined by scanning electron microscopy (SEM, Sigma 500, Zeiss, Germany) and energy dispersive spectroscopy (EDS, X-MAX 50, Oxford, U.K.). The pore structure of TiSO-REM was characterized by mercury intrusion porosimetry (MIP, AutoPore® V, Micromeritics, U.S.A.). Fourier transform infrared spectroscopy (FT-IR) was used to characterize the functional groups involved in the surface layer of TiSO-REM electrode before and after electrochemical degradation of 4-CP.

2.3. Experimental Setup and Operation

The electrolytic system was operated under a dead-end filtration mode (Fig. S1). The permeate was collected and recycled back to the reactor by a peristaltic pump (BT100-2J, Baoding Shenchen

Precision Pump Co. Ltd, China). The TiSO-REM anode was placed in the middle of the reactor with the flexible SS cathode surrounding it. The anode potential was measured versus Ag/AgCl reference electrode (0.195 V vs SHE) and reported versus standard hydrogen electrode (SHE). The supporting electrolyte was $NaClO_4$ solution (50 mmol L^{-1}). An ultrasound vibrator (Skymen Cleaning Equipment Shenzhen Co. Ltd) with a nominal power of 180 W and a frequency of 28 kHz was fixed to the bottom of the reactor. The current density of 0-20 mA cm^{-2} was applied to the TiSO-REM EO system under constant-current mode by direct current (DC) power supply (HSPY-60-5, Hanshengpuyuan, China). During cyclic tests, each cycle was conducted under potential of 3 V vs SHE for 40 min based on a solution volume of 1 L. Following each cycle, the TiSO-REM was cleaned with DI-water by recirculation using peristaltic pump for 20 min.

2.4. Analyses and Calculations

4-chlorophenol (4-CP) and degradation products were determined by using ultra-performance liquid chromatography-mass spectrometry/mass spectrometry (UPLC-MS/MS , Waters Co., Milford, MA, U.S.A.) equipped with a Symmetry® C18 column (1.7 μm, 2.1 mm×50 mm, Waters, MA). 0.1% formic acid-acetonitrile (60:40, v/v) was used as the mobile phase at a flow rate of 0.1 mL min^{-1}. The MS data was obtained in a positive electrospray ionization (ESI) mode by full scan mass spectrum with m/z ratio in the range of 80-520. Chemical oxygen demand (COD) was determined by using a COD analyzer (5B-3B (V8), Lianhuakeji, Beijing, China). The electrochemical properties of TiSO-REM were tested by using linear sweep voltammetry (LSV), electrochemical impedance spectroscopy (EIS) and amperometric *i-t* curve using galvanostat (CHI750D, CH Instruments, Inc., USA). Hydroxyl radicals (•OH) produced in EO process were identified by using ESR (A200,

Bruker, Germany).

In order to examine the effect of ultrasound on TiSO-REM EO system, the mass transfer constant ($k_{m,i}$) was calculated based on measurement of limiting current for $Fe(CN)_6^{3-}$ reduction (Eqs. 5 and 6). The filtration experiment was conducted in the electrolyte containing 5 mmol L^{-1} $K_4[Fe(CN)_6]$, 10 mmol L^{-1} $K_3[Fe(CN)_6]$, and 100 mmol L^{-1} KH_2PO_4 [30, 38].

$$Fe(CN)_6^{3-} + e^- \rightarrow Fe(CN)_6^{4-} \tag{5}$$

$$k_m = \frac{I_{\lim}}{nAFC} \tag{6}$$

where I_{lim} (A) is the limiting current, n (n=1) the number of transferred electron, A (m^2) the geometric area of anode, F (96485 C mol^{-1}) the Faraday constant, C (5 mmol L^{-1}) the bulk concentration of $Fe(CN)_6^{4-}$. The removal efficiency was calculated according to Eq. 7. The removal of 4-CP and COD was assumed to follow the pseudo first-order kinetics according to

$$\alpha_i = \frac{\left(C_{0,i} - C_{t,i}\right)}{C_{0,i}} \times 100\% \tag{7}$$

$$k_{s,i} = -\frac{\ln(C_{t,i} / C_{0,i})}{t} \tag{8}$$

where $C_{0,i}$ (mg L^{-1}) and $C_{t,i}$ (mg L^{-1}) are the initial concentration and the concentration after a electrolysis time t (min), and $k_{s,i}$ (min^{-1}) the reaction rate constant. In order to determine the synergistic effect of EO-US system, the enhancement factor f_e was defined as

$$f_e = \frac{k_{EO-US}}{k_{EO} + k_{US}} \times 100\% \tag{9}$$

The energy consumption (EC) can be calculated by

$$\text{EC (kWh kg}^{-1}\text{ COD)} = \frac{Pt}{60V(COD_0 - COD_t)} \tag{10}$$

where P (kW) is the power, V (L) the volume of the treated solution, COD_0 (kg L^{-1}) and COD_t (kg

L^{-1}) the initial and the final COD values of the solution, respectively. The power of EO (P_{EO}) was measured based on the cell voltage and the current, while the transmitted power of US (P_{US}) was determined by calorimetry [39] according to

$$P_{US} = mC_p(\frac{\mathrm{d}T}{\mathrm{d}t}) \tag{11}$$

where m (0.0045 kg) is the mass of water in the REM pores, C_p the specific heat capacity of water (4.18 kJ K^{-1} kg^{-1}), and dT/dt (0.067 K s^{-1}) the temperature increase per second at the beginning of the test.

2.5. Simulations

The computational models are established as follows. The simulation numerically underlined the effect of ultrasound on electrochemical reaction, mass transfer and permeate flux of TiSO-REM anode in EO process using Helmholtz equations as [24, 40, 41].

$$\nabla \cdot \left(-\frac{1}{\rho_c} \nabla p \right) - \frac{\omega^2}{\rho_c c_c^{\,2}} p = 0 \tag{12}$$

$$-\vec{n} \cdot (-\frac{1}{\rho_c} \nabla p) = -p \frac{i\omega}{Z_i} \tag{13}$$

where p (Pa) is the acoustic pressure, ω/c (c_c=c is the sound speed, m s^{-1}) the wave number k (m^{-1}). ρ (ρ_c=ρ, kg m^{-3}), $\vec{n}$ and Z_i=$\rho_0 c_0$ are the density, unit normal vector at boundary and the acoustic impedance of external media. The flow dynamics were modeled by classical Navier-Stokes equations

$$\rho(\vec{u} \cdot \nabla)\vec{u} = \nabla \cdot [-\rho \vec{I} + \mu(\nabla \vec{u} + (\nabla \vec{u})^T)] + F \tag{14}$$

$$\rho \nabla \cdot (\vec{u}) = 0 \tag{15}$$

where $\vec{u}$ (m s^{-1}), μ (Pa s), and T (K) are the velocity vector, the dynamic viscosity of liquid, and the absolute temperature, and F (N m^{-3}) the volume force vector could be written as

$$F_v = \frac{2\alpha}{\rho_e c_e^{\,2}} |p|^2 \tag{16}$$

where α (m^{-1}) is the absorption coefficient, ρ_e and c_e the density and ultrasound velocity of electrolyte. The mass transfer can be described as

$$\frac{\partial C_i}{\partial t} = D\nabla^2 C_i - \nabla u C_i \tag{17}$$

$$J_{0,C} = \frac{j}{nF} \tag{18}$$

$$k_m = -\frac{D}{(C_{0,i} - C_{t,i})} \frac{dC}{dx}\Big|_{x=0} \tag{19}$$

where D (0.63×10^{-9} m^2 s^{-1}) is the diffusion coefficient of $Fe(CN)_6^{4-}$, $J_{0,C}$ and j the mass flux of the electrode surface and the anodic current density. j was obtained from the limiting current method and $J_{0,C}$ was calculated by Eq. 18 for models to simulate concentration distribution. The calculated mass transfer coefficients by Eq. 19 could be compared with the results obtained from limiting current experiment (Eq. 6).

The theoretical calculations based on DFT was performed on a Gaussian 09 package using the 6-31+ g(d) basis set for frequency and geometry optimizations and the 6-311++g(3df, 2p) basis set for energy calculations. B3lyp function was used for exchange and correlation. The E^0 values and activation energy ($\Delta G^{\ddagger}$) for direct electron transfer (DET) reaction could be obtained according to Marcus theory as

$$E^0 = -\frac{\Delta_r G^o}{nF} - E_{abs}^0 \text{(SHE)} \tag{20}$$

$$\Delta G^{\ddagger} = \frac{\lambda_f}{4}\left[1 - \frac{96.5(E - E^0)}{\lambda_f}\right]^2 \tag{21}$$

where $\Delta_r G^o$ is the standard free energy of the reduction reaction, $E_{abs}{}^0$ (SHE, 4.28 V) the reference value of absolute standard reduction potential of SHE, λ_f the total reorganization energy of the

oxidation reaction and E (V) the applied electrode potential.

3. Results and Discussion

3.1. Characterization of TiSO-REM Anode

The crystalline structure and phase composition of TiSO-REM were characterized by using XRD and XPS techniques. As illustrated in Fig. 1a, Ti_4O_7 could be identified by the characteristic peaks at the diffraction angles of 20.8°, 27.8°, 29.6°, 31.6°, 36.2°, and 55.1° (JCPDS No.500787). In addition, the presence of Ti_5O_9 crystal was also shown by 2θ=40.4° and 57.9°. High-resolution XPS spectra exhibited the existence of Ti^{4+} and Ti^{3+} peaks in association with mismatch of the lattice in TiSO-REM (Fig. 1b) [36, 37, 42]. SEM image of TiSO-REM (Fig. 1c) reveals a rough surface with abundant irregular pores formed by TiSO particles, which increased the specific surface area and inner pore volume of REM. As indicated by cumulative pore area and differential intrusion of Hg porosimetry measurement, the TiSO-REM had a median pore diameter of 0.5081 μm, porosity of 29.22% and total pore area of 0.316 m^2 g^{-1} (Figs. 1d and 1e). The macro-scale pores allowed effective penetration of dissolved species across the membrane, during which sufficient contact between electrode and pollutants could be achieved. Furthermore, EIS was performed to estimate electrochemically active surface area (ECSA) of TiSO-REM anode at potential of 0.6 V vs SHE (open circuit voltage) and a frequency range of 10^{-2} to 10^5 Hz [42]. Fig. 1f shows the charge transfer resistance (R_p) of 29.68±0.19 Ω and solution resistance (R_s) of 5.362±0.01 Ω, respectively. The ECSA could be derived from double-layer capacitances (C_{dl}, F) as

$$C_{dl} = \left(\frac{T}{\left[R_S^{-1} + R_p^{-1} \right]^{1-\varnothing}} \right)^{1/\varnothing} \tag{22}$$

$$\mathrm{ECSA} = \frac{C_{dl}}{C_{dl,0}} \tag{23}$$

where T (0.0205579) is the constant associated with the constant phase element (CPE), $\varnothing$ (-0.74531) is equal to -pΠ/2 according to the angle of rotation on the complex plane plots. The value obtained for double-layer capacitance ($C_{dl,0}$) of the metal oxide surface was assumed to be 60 μF cm^{-2} [43], on the basis of which the ECSA of TiSO-REM was calculated to be 8.83±0.06 m^2.

Fig. 1 (a-f)

3.2. Permeate Flux and Mass Transfer

The permeate flux was shown to be increased when transmembrane pressure (TMP) was elevated from 0.005 MPa to 0.025 MPa, primarily due to an increased driving pressure applied to REM (Figs. 2a and 2b). There is an observation of similar water flux values for initial anode potential of 0 V and 1 V vs SHE (5.0×10^3 L m^{-2} h^{-1}, taking Fig. 2b as an example), whereas further increasing anode potential to 3 V vs SHE led to approximately 42% decline in permeate flux (2.9×10^3 L m^{-2} h^{-1}). Hypothetically, we attributed OER to be the major factor responsible for difference in permeate flux with respect to anode potential. Since the potential higher than 1 V vs SHE is requisite for OER thermodynamically, no oxygen gas was produced electrochemically at anode potential lower than 1 V vs SHE. In this case, aqueous solution was filtered through the inner pores of REM in the absence of oxygen evolution. As shown in Fig. S2b, the development of OER resulted in formation of oxygen bubbles with an average diameter of d_{O2}=0.4 mm at anode potential of 3 V vs SHE. The oxygen bubbles grew gradually in size followed by being trapped in the confined

space of the microporous flow channels, which should be the most likely reason for decline in cross section of flow channel. This would cause an increase in local pressure and decrease in local flow velocity and water flux within micro-porous flow channel under OER condition (i. e. anode potential of 3 V vs SHE) unless external driving pressure could be further increased. Such assumption could be verified by modeling data of spatial distribution of local velocity and pressure within the flow channel of REM with and without oxygen bubbles in the absence and presence of ultrasound application by using COMSOL software (Figs. 2d-2f). As shown in Fig. 2c, applying ultrasound (180 W) to REM recovered permeate flux by 59% to 4.6×10^3 L m^{-2} h^{-1} at anode potential of 3 V vs SHE, a value only 8% lower than that without OER (0 V and 1 V vs SHE). Accordingly, the size in diameter of oxygen bubbles was shown to be decreased to d_{O2}=0.15 mm on average (Fig. S2c).

The COMSOL simulation profiles also displayed a dramatically higher local flow velocity and permeate flux for d_{O2}=0.15 mm (4.5×10^3 L m^{-2} h^{-1}) than that for d_{O2}=0.4 mm (3.1×10^3 L m^{-2} h^{-1}). Both experimental and theoretical results clearly confirmed an enhanced permeation flux of TiSO-REM assisted by application of ultrasound to EO process. Besides, O_2 bubbles evolved in EO-US detached from the anode surface at a rate much faster than that in EO. The simulation revealed that the velocity of channel flow at 0 V vs SHE was 4.72×10^{-3} m s^{-1} on average (Fig. 2d). In contrast, a large amount of oxygen bubbles evolved at anode/solution interface within the porous structure at 3 V vs SHE, which greatly suppressed the volume available for water permeation by blocking the channels (Fig. 2e), and thus resulted in 38.6% decrease in mean velocity to 2.90×10^{-3} m s^{-1}. Specifically, when the size of O_2 bubbles grew up to a critical value (departure diameter), they would depart from the anode surface under the combined actions of inertia, buoyancy and hydrodynamic shear stress. The amount of newly formed bubbles and those flushed out of

micropores reached an equilibrium quickly [44], providing the most likely explanation to initial decline followed by subsequent steady state (2.9×10^{3} L m^{-2} h^{-1}) at 3 V vs SHE (Fig. 2b). Ultrasound created a stronger turbulence and enhanced shear stress promoting the O_2 bubbles to collapse to smaller ones (Fig. 2f), which made them flushed out of the pores more easily for permeate flow [45]. Besides that, the O_2 bubbles evolved were conducive to produce cavitation bubbles that could be damaged under the effect of ultrasound [14, 46]. In this way, a new steady state of smaller oxygen volume could be achieved, resulting in a lower resistance to water permeation and a significant recovery of permeate flux (4.6×10^{3} L m^{-2} h^{-1}) with velocity of 4.24×10^{-3} m s^{-1} on average (Figs. 2c and 2f).

Fig. 2 (a-f)

Applying ultrasound could mitigate the retention of O_2 bubbles in the porous structures by destructing large-size bubbles, and thus not only increase permeate flux but also promote local mass transfer. Fig. S3 illustrates the k_m values for EO (0.912×10^{-5} m s^{-1}, 1.295×10^{-5} m s^{-1}, and 1.866×10^{-5} m s^{-1}) and EO-US (1.931×10^{-5} m s^{-1}, 2.745×10^{-5} m s^{-1}, 3.465×10^{-5} m s^{-1}) under different TMP of 0.005, 0.025, and 0.06 MPa. The k_m was increased with the TMP for both cases, and significantly higher k_m values were obtained for EO-US. The velocity of microchannel flow increased with the TMP due to enhanced driving force for mass transport (Fig. 2). The cavitation effect produced by ultrasound improved the turbulence of convective flow in the inner microstructure of REM.

3.3. Electrochemical Oxidation of 4-CP

To further demonstrate the effect of ultrasound on organic oxidation, the removal of 4-CP in EO and EO-US were investigated at different anodic potentials under dead-end filtration mode. First, the reaction rate constant in individual ultrasound system (k_{US}) was determined to be 0.0049 min^{-1}. At low potential of 1 V vs SHE, the 4-CP reaction rate constants were determined to be k_{EO}=0.0008 min^{-1} and $k_{EO\text{-}US}$=0.0059 min^{-1} for EO and EO-US, respectively, with f_e of 1.04 (Fig. 3a). The slight removal of 4-CP in EO should be attributed to electro-adsorption by the anode instead of electrochemical oxidation, while its degradation in EO-US mainly originated from indirect oxidation by •OH produced from cavitation effect. Higher potential (2.0 V vs SHE) initiated DET oxidation of 4-CP shown by increased k_{EO} to 0.0074 min^{-1} (Fig. 3b). Owing to the formation of $[4\text{-CP}]^{\bullet+}$ by DET reaction, the positively charged intermediate reacted more easily with •OH in EO-US (details in Section 3.4), which resulted in triple increase in $k_{EO\text{-}US}$ (0.0195 min^{-1}) compared with that obtained at potential of 1.0 V vs SHE and an increased f_e (1.59). When the potential was increased to 3.0 V vs SHE, the •OH generated by the TiSO-REM anode allowed enhanced removal of 4-CP (k_{EO}=0.0258 min^{-1}) though the produced O_2 bubbles might hinder mass transport in the pores (Fig. 3c). For EO-US, the cavitation effect greatly alleviated the bubble blockage and improved the •OH production, leading to approximately 261% increase in $k_{EO\text{-}US}$ value (0.0932 min^{-1}) compared with that for EO and a significantly enhanced f_e (3.04). Therefore, an enhanced removal of 4-CP could be achieved by the synergistic effect offered by sonoelectrochemistry, which was consistent with previous studies on graphite, dimensionally stable anode (DSA) and boron doped diamond (BDD) in EO system [47-49].

Fig. 3 (a-c)

3.4. Mechanisms for Electrochemical Oxidation

The current response of TiSO-REM for EO and EO-US was investigated under potentiostatic mode (2.0 V vs SHE). As shown in Figs. 4a and 4b, the current wave represents the diffusion current on the anode surface. Upon injection of 4-CP, the diffusion layer was formed by diffusion of part of 4-CP onto the surface of TiSO-REM, which produced step pulse signals by electrolysis occurring under limit current. When the injection was repeated, the peak current re-appeared with the formation of new step of current response. For sonoelectrochemistry where ultrasound was introduced, the rate at which 4-CP diffused onto the anode was promoted by suppressing diffusion layer on the surface of TiSO-REM.

Fig. 4. (a-e)

At anode potential higher than 3.0 V vs SHE, several oxidative radical species may be produced from water oxidation [2]. Thus, the formation of radical species was identified by using ESR technique on a qualitative basis (Figs. 4c-4e). With 5,5-dimethyl-1-pyrroline N-oxide (DMPO) serving as trap agent, the quartet lines with peak strength of 1:2:2:1 hyperfine coupling constant of α_N=1.49 mT and α_H=1.49 mT (*g*-factor of 2.0055) could be observed in ESR spectra for both EO and EO-US process. This is the representative of characteristic signals of DMPO-OH adduct being identical to that found in typical Fenton reaction, indicating the formation of •OH from water oxidation on TiSO-REM anode. The ability of producing •OH by TiSO electrode should result from the oxygen evolution potential (2.5 V vs SHE) as great as that of BDD anode, which has been

evidenced in many previous studies [37, 42, 50]. Based on external standard agent 2,2,6,6-tetramethylpiperidine-1-oxyl (TEMPO) (Fig. S4), •OH concentration could be quantified to be 176.12 μM in EO-US, accounting for a value more than two times of that found in EO (85.78 μM), and approximately six times of that in individual ultrasound system (29.78 μM). The enhanced performance by sonoelectrochemistry may be attributed to several reasons. First, the introduction of ultrasound can achieve enhanced local turbulence of the solution and stronger diffusion/desorption effects of O_2 bubbles [51], which lowered the interfacial resistance of solution/electrode (Fig. S5). Second, the collapse of the cavitation bubbles creates a harsh micro-environment of extremely high local temperature and pressure [47, 52]. Since only dissolved oxygen (DO) in the solution can be active for ultrasonic cavitation, relatively low DO concentration (<2.0 mg O_2 L^{-1}) only yielded DMPO-OH signals with low strength for individual ultrasound system. In contrast, water electrolysis assisted by sonoelectrochemistry produced a larger amount of oxygen bubbles, and thus a significantly increased •OH production. Last, gas like oxygen generated at higher potentials has the ability of trapping electrons to form superoxide radicals and H_2O_2, which in turn can be converted into •OH under ultrasound condition (Eqs. S1-S8) [53, 54]. Therefore, an enhanced production of •OH should be responsible for 4-CP oxidation and COD removal in EO-US process.

Fig. 5 (a, b)

Next, we used DFT calculations to theoretically underline the mechanisms for 4-CP oxidation in EO-US (DET or indirect •OH oxidation). $\Delta G^{\ddagger}$ values, activation energy (E_a) and potential for DET oxidation of 4-CP could be calculated at anode potential of 3.0 V vs SHE based on Eqs. 20 and 21.

As shown in Fig. 5a, E_a value for 4-CP oxidation approached almost 0 kJ mol^{-1} at anode potential of 1.66 V vs SHE, a value much lower than 2.38 V vs SHE for •OH production. The theoretical data in combination with LSV results (Fig. S6) confirmed the thermodynamic possibility of DET oxidation for 4-CP before •OH formation. DET process led to the loss of one electron to the anode, forming transient positively charged $[4\text{-CP}]^{\bullet+}$ cationic radical. The DFT calculations also determined the free energies of reaction associated with 4-CP, $[4\text{-CP}]^{\bullet+}$ and •OH. As given in Eqs. 24 and 25 as well as Fig. 5b, the free energy of rate-limiting step was 17 kJ mol^{-1} for the reaction between •OH and 4-CP (ΔG_1) to form the transition state (TS1). Following dehydration and •OH addition reaction, the transient 4-CP-OH was produced with free energy of -406 kJ mol^{-1}. This may explain the reason for low reaction rate of 4-CP observed (Fig. 3a) in individual ultrasound system where the •OH was available. The values of free energy below zero allowed the reaction between $[4\text{-CP}]^{\bullet+}$ and •OH to be more thermodynamically favorable than that between 4-CP and •OH (Figs. 5a and 5b), which was consistent with previous studies [7, 30]. Once $[4\text{-CP}]^{\bullet+}$ was formed, it would undergo further •OH oxidation to hydroquinone, benzoquinone and aliphatic carboxylic acids via hydroxylation, dehydrogenation and ring opening, followed by eventually being mineralized to CO_2, H_2O and Cl^- according to the mechanisms reported in detail in previous studies [34, 35]. That is, the enhanced oxidation of 4-CP could be achieved through combining anodic DET oxidation and subsequent •OH-mediated oxidation facilitated by water oxidation and cavitation effect in sonoelectrochemical system.

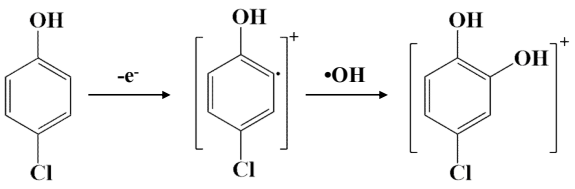

(24)

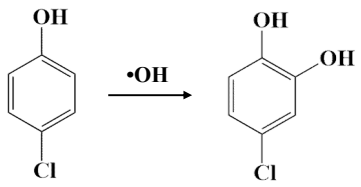

(25)

3.5. Stability and Durability

In order to evaluate the stability and durability of TiSO-REM anode in the absence and presence of ultrasound, cyclic tests were carried out using real 4-CP containing wastewater (COD of 338 mg L^{-1}, pH 7.07, conductivity of 25.4 mS cm^{-1} and 4-CP concentration of 28 mg L^{-1}) collected from the brine stream of electrodialysis (ED) process in a local petrochemical wastewater treatment plant. As shown in Fig. 6a, during 100-cycle phase of tests, COD removal was shown to be decreased gradually from 65.8% to 38.4% (by approximately 27%) in EO, whereas the removal was maintained in the range of 87.81%-88.95% in EO-US system. The long-term stability of EO-US was improved substantially in comparison with that of EO. The energy consumption of EO-US (9.5 kWh kg^{-1} COD) was calculated to be slightly higher than that of EO (6.4 kWh kg^{-1} COD) in the first cycle. However, the energy consumption increased rapidly for EO due to its poor stability of COD removal in long-term operation, to be specific, 10.8 kWh kg^{-1} COD for EO and 10.1 kWh kg^{-1} COD for EO-US in the 100th cycle. Besides, the transmitted ultrasonic power (1.26 W) only accounted for a very small fraction of the electrical power of the ultrasound vibrator due to the energy dissipation in the current system. Therefore, the EO-US system needs to be further optimized in practical applications for higher degradation rate and improved energy efficiency.

For EO, the loss of electrochemical activity of TiSO-REM was assumed to result from deactivation associated with electrode fouling. The SEM image shows that the surface of pristine

TiSO-REM anode was made of smooth agglomerates of uniformly-sized particles, and the particle-particle bonding resulted in the formation of porous structure in the cavity (Fig. 1c). After electrolysis for 100 cycles without ultrasound, the anode surface was obviously contaminated by a large amount of dispersed floc-shaped foulants that might be produced from electro-polymerization of 4-CP during electrolysis (Fig. 6d). The electrode deactivation and fouling were also commonly observed for BDD anode in prior studies on oxidation of recalcitrant organic pollutants [27, 55-58]. On the contrary, the degree to which anode was polluted in EO-US could be much alleviated compared with that in EO, indicating the positive function of ultrasound in controlling the anode fouling and prolonging the lifetime of anode material (Fig. 6c). In addition, the integrity of REM anode was observed under the application of ultrasound for 100-cycle tests, demonstrating good mechanical durability for long term use in EO-US. EDS data given in Fig. 6b reveals the presence of C and Cl element due to breakage and polymerization/adsorption of 4-CP on the anode surface in EO, and the content of C, O and Cl element in EO was higher than that in EO-US. The application of ultrasound allowed more efficient degradation of 4-CP and enhanced local mass transfer, and thus a lower possibility of electrolytic polymerization on the anode surface of TiSO-REM.

Furthermore, FT-IR technique was also used to characterize the functional groups involved in fouling layer on the TiSO-REM anode during 4-CP oxidation. As illustrated in Figs. 6e-6g, the characteristic peaks found at 3350 and 3177 cm^{-1} accounted for the stretching of the N-H bonds, while those observed at 1657 and 1631 cm^{-1} should be assigned to the stretching of C=O bonds. The peaks are characteristic of different substituent linked to the benzene ring, e. g. COOH groups at 1425 cm^{-1} and 1414 cm^{-1}, and out-of-plane bending of COH at 945 cm^{-1}, 910 cm^{-1} and 882 cm^{-1}, respectively. These results clearly suggested the formation of organic polymerization layer on the

TiSO-REM anode [59]. Notably, the strength of these characteristic peaks was lowered substantially or even disappeared in EO-US system, which also confirmed the alleviation of anode deactivation and fouling assisted by ultrasound.

Fig. 6. (a-g)

4. Conclusions

Based on above results, the main conclusions of this study can be drawn as follows. Ultrasound could alleviate the retention of O_2 bubbles in the porous structures by destructing large-size bubbles, and thus not only increased permeate flux but also promoted local mass transfer. Oxidation rate of 4-CP for EO-US was 216% higher than that for EO, due to enhanced mass transfer and •OH production under the cavitation effect of ultrasound. DFT calculations confirmed the most efficient pathway of 4-CP removal to be DET reaction of 4-CP to form $[4\text{-CP}]^{\bullet+}$, followed by subsequent oxidation mediated by •OH produced from anodic water oxidation on TiSO-REM anode. The stability of TiSO-REM could be improved considerably by application of ultrasound, due to alleviation of electrode deactivation and fouling, indicated by cyclic test, SEM observation and FT-IR characterization. This study provides a proof-of-concept demonstration of ultrasound for enhanced EO of recalcitrant organic pollutants by REM anode, making decentralized wastewater treatment more efficient and more reliable.

Acknowledgements

Project supported by the National Natural Science Foundation of China (Grant No. 51822806,

51678184, 51761145031), Singapore National Research Foundation (Grant No. NRF2017NRF-NSFC001-048), Fundamental Research Funds for the Central Universities (Grant No. HIT.BRETIV.201905), and State Key Laboratory of Urban Water Resource and Environment (Harbin Institute of Technology) (No. 2020DX07). Many thanks go to Mr. Yibing Huang (Ti-dynamics Co. Ltd, China) for providing TiSO-REM electrode during the course of this study.

References

[1] C.A. Martinez-Huitle, S. Ferro, Electrochemical oxidation of organic pollutants for the wastewater treatment: Direct and indirect processes, Chem. Soc. Rev. 35 (2006) 1324-1340. https://doi.org/10.1039/b517632h.

[2] M. Panizza, G. Cerisola, Direct and mediated anodic oxidation of organic pollutants, Chem. Rev. 109 (2009) 6541-6569. https://doi.org/10.1021/cr9001319.

[3] T.X.H. Le, H. Haflich, A.D. Shah, B.P. Chaplin, Energy-efficient electrochemical oxidation of perfluoroalkyl substances using a Ti_4O_7 reactive electrochemical membrane anode, Environ. Sci. Technol. Let. 6 (2019) 504-510. https://doi.org/10.1021/acs.estlett.9b00397.

[4] Z. Pan, C. Song, L. Li, H. Wang, Y. Pan, C. Wang, J. Li, T. Wang, X. Feng, Membrane technology coupled with electrochemical advanced oxidation processes for organic wastewater treatment: Recent advances and future prospects, Chem. Eng. J. 376 (2019) 120909. https://doi.org/10.1016/j.cej.2019.01.188.

[5] S. Almassi, Z. Li, W. Xu, C. Pu, T. Zeng, B.P. Chaplin, Simultaneous adsorption and electrochemical reduction of N-nitrosodimethylamine using carbon-Ti_4O_7 composite reactive electrochemical membranes, Environ. Sci. Technol. 53 (2019) 928-937.

https://doi.org/10.1021/acs.est.8b05933.

[6] L. Guo, K. Ding, K. Rockne, M. Duran, B.P. Chaplin, Bacteria inactivation at a sub-stoichiometric titanium dioxide reactive electrochemical membrane, J. Hazard. Mater. 319 (2016) 137-146. https://doi.org/10.1016/j.jhazmat.2016.05.051.

[7] P. Gayen, C. Chen, J.T. Abiade, B.P. Chaplin, Electrochemical oxidation of atrazine and clothianidin on Bi-doped SnO_2-Ti_nO_{2n-1} electrocatalytic reactive electrochemical membranes, Environ. Sci. Technol. 52 (2018) 12675-12684. https://doi.org/10.1021/acs.est.8b04103.

[8] Y. Jing, L. Guo, B.P. Chaplin, Electrochemical impedance spectroscopy study of membrane fouling and electrochemical regeneration at a sub-stoichiometric TiO_2 reactive electrochemical membrane, J. Membr. Sci. 510 (2016) 510-523. https://doi.org/10.1016/j.memsci.2016.03.029.

[9] C. Trellu, C. Coetsier, J.C. Rouch, R. Esmilaire, M. Rivallin, M. Cretin, C. Causserand, Mineralization of organic pollutants by anodic oxidation using reactive electrochemical membrane synthesized from carbothermal reduction of TiO_2, Water Res. 131 (2018) 310-319. https://doi.org/10.1016/j.watres.2017.12.070.

[10] H. Vogt, R.J. Balzer, The bubble coverage of gas-evolving electrodes in stagnant electrolytes, Electrochim. Acta 50 (2005) 2073-2079. https://doi.org/10.1016/j.electacta.2004.09.025.

[11] S.I. Hatanaka, T. Taki, M. Kuwabara, M. Sano, S. Asai, Effect of process parameters on ultrasonic separation of dispersed particles in liquid, Jpn. J. Appl. Phys. 38 (1999) 3096-3100. https://doi.org/10.1143/JJAP.38.3096.

[12] R. Haghayeghi, H. Bahai, P. Kapranos, Effect of ultrasonic argon degassing on dissolved hydrogen in aluminium alloy, Mater. Lett. 82 (2012) 230-232. https://doi.org/10.1016/j.matlet.2012.05.112.

[13] T. Kondo, J. Gamson, J.B. Mitchell, P. Riesz, Free radical formation and cell lysis induced by ultrasound in the presence of different rare gases, Int. J. Radiat. Biol. 54 (1988) 955-962. https://doi.org/10.1080/09553008814552351.

[14] L. Liu, Y. Yang, P. Liu, W. Tan, The influence of air content in water on ultrasonic cavitation field, Ultrason. Sonochem. 21 (2014) 566-571. https://doi.org/10.1016/j.ultsonch.2013.10.007.

[15] X. Liu, Z. Zhang, W. Hu, Q. Le, L. Bao, J. Cui, J. Jiang, Study on hydrogen removal of AZ91 alloys using ultrasonic argon degassing process, Ultrason. Sonochem. 26 (2015) 73-80. https://doi.org/10.1016/j.ultsonch.2014.12.015.

[16] J.L. Hardcastle, J.C. Ball, Q. Hong, F. Marken, R.G. Compton, S.D. Bull, S.G. Davies, Sonoelectrochemical and sonochemical effects of cavitation: Correlation with interfacial cavitation induced by 20 kHz ultrasound, Ultrason. Sonochem. 7 (2000) 7-14. https://doi.org/10.1016/s1350-4177(99)00026-7.

[17] R.G. Compton, J.C. Eklund, F. Marken, Sonoelectrochemical processes: A review, Electroanalysis 9 (1997) 509-522. https://doi.org/10.1002/elan.1140090702.

[18] F. Mendez-Arriaga, R.A. Torres-Palma, C. Petrier, S. Esplugas, J. Gimenez, C. Pulgarin, Ultrasonic treatment of water contaminated with ibuprofen, Water Res. 42 (2008) 4243-4248. https://doi.org/10.1016/j.watres.2008.05.033.

[19] X. Zhu, J. Ni, H. Li, Y. Jiang, X. Xing, A.G.L. Borthwick, Effects of ultrasound on electrochemical oxidation mechanisms of p-substituted phenols at BDD and PbO_2 anodes, Electrochim. Acta 55 (2010) 5569-5575. https://doi.org/10.1016/j.electacta.2010.04.072.

[20] M.J.M.D. Vidales, M.P. Castro, C. Sáez, P. Cañizares, M.A. Rodrigo, Radiation-assisted electrochemical processes in semi-pilot scale for the removal of clopyralid from soil washing wastes,

Sep. Purif. Technol. 208 (2018) 100-109. https://doi.org/10.1016/j.seppur.2018.04.074.

[21] B. Thokchom, A.B. Pandit, P. Qiu, B. Park, J. Choi, J. Khim, A review on sonoelectrochemical technology as an upcoming alternative for pollutant degradation, Ultrason. Sonochem. 27 (2015) 210-234. https://doi.org/10.1016/j.ultsonch.2015.05.015.

[22] J. Klima, Application of ultrasound in electrochemistry. An overview of mechanisms and design of experimental arrangement, Ultrasonics 51 (2011) 202-209. https://doi.org/10.1016/j.ultras.2010.08.004.

[23] F. Trabelsi, H. Aït-Lyazidi, B. Ratsimba, A.M. Wilhelm, H. Delmas, P.L. Fabre, J. Berlan, Oxidation of phenol in wastewater by sonoelectrochemistry, Chem. Eng. Sci. 51 (1996) 1857-1865. https://doi.org/10.1016/0009-2509(96)00043-7.

[24] M. Zhao, L. Du, C. Du, Z. Wei, X. Ji, Z. Bai, X. Liu, Quantitative study of mass transfer in megasonic micro electroforming based on mass transfer coefficient: Simulation and experimental validation, Electrochim. Acta 297 (2019) 328-333. https://doi.org/10.1016/j.electacta.2018.12.018.

[25] N. Neha, M.H. Islam, S. Baranton, C. Coutanceau, B.G. Pollet, Assessment of the beneficial combination of electrochemical and ultrasonic activation of compounds originating from biomass, Ultrason. Sonochem. 63 (2020) 104934. https://doi.org/https://doi.org/10.1016/j.ultsonch.2019.104934.

[26] P.L.B. Ferrández, M.D. Esclapez, V.S. Bernal, J. González-García, Sonoelectrochemistry in environmental applications, in: B.G. Pollet (Ed.), Power Ultrasound in Electrochemistry, 2012, pp. 101-139.

[27] J. Theerthagiri, J. Madhavan, S.J. Lee, M.Y. Choi, M. Ashokkumar, B.G. Pollet, Sonoelectrochemistry for energy and environmental applications, Ultrason. Sonochem. 63 (2020)

104960. https://doi.org/https://doi.org/10.1016/j.ultsonch.2020.104960.

[28] L. Guo, Y. Jing, B.P. Chaplin, Development and characterization of ultrafiltration TiO_2 magneli phase reactive electrochemical membranes, Environ. Sci. Technol. 50 (2016) 1428-1436. https://doi.org/10.1021/acs.est.5b04366.

[29] S.O. Ganiyu, N. Oturan, S. Raffy, M. Cretin, C. Causserand, M.A. Oturan, Efficiency of plasma elaborated sub-stoichiometric titanium oxide (Ti_4O_7) ceramic electrode for advanced electrochemical degradation of paracetamol in different electrolyte medium, Sep. Purif. Technol. 208 (2018) 142-152. https://doi.org/10.1016/j.seppur.2018.03.076.

[30] A.M. Zaky, B.P. Chaplin, Mechanism of p-substituted phenol oxidation at a Ti_4O_7 reactive electrochemical membrane, Environ. Sci. Technol. 48 (2014) 5857-5867. https://doi.org/10.1021/es5010472.

[31] A.M. Zaky, B.P. Chaplin, Porous substoichiometric TiO_2 anodes as reactive electrochemical membranes for water treatment, Environ. Sci. Technol. 47 (2013) 6554-6563. https://doi.org/10.1021/es401287e.

[32] Q. Ma, H. Zhang, X. Deng, Y. Cui, X. Cheng, X. Li, M. Xie, Q. Cheng, B. Li, Electrochemical fabrication of NZVI/TiO_2 nano-tube arrays photoelectrode and its enhanced visible light photocatalytic performance and mechanism for degradation of 4-chlorphenol, Sep. Purif. Technol. 182 (2017) 144-150. https://doi.org/10.1016/j.seppur.2017.03.047.

[33] M. Tian, S.S. Thind, J.S. Dondapati, X. Li, A. Chen, Electrochemical oxidation of 4-chlorophenol for wastewater treatment using highly active UV treated TiO_2 nanotubes, Chemosphere 209 (2018) 182-190. https://doi.org/10.1016/j.chemosphere.2018.06.042.

[34] Z. Yang, X. Zhang, S. Pu, R. Ni, Y. Lin, Y. Liu, Novel Fenton-like system (Mg/Fe-O_2) for

degradation of 4-chlorophenol, Environ. Pollut. 250 (2019) 906-913. https://doi.org/10.1016/j.envpol.2019.04.096.

[35] Z. Huang, Z. Chen, Y. Chen, Y. Hu, Synergistic effects in iron-copper bimetal doped mesoporous gamma-Al_2O_3 for Fenton-like oxidation of 4-chlorophenol: Structure, composition, electrochemical behaviors and catalytic performance, Chemosphere 203 (2018) 442-449. https://doi.org/10.1016/j.chemosphere.2018.04.001.

[36] G. Liu, H. Zhou, J. Teng, S. You, Electrochemical degradation of perfluorooctanoic acid by macro-porous titanium suboxide anode in the presence of sulfate, Chem. Eng. J. 371 (2019) 7-14. https://doi.org/10.1016/j.cej.2019.03.249.

[37] S. You, B. Liu, Y. Gao, Y. Wang, C.Y. Tang, Y. Huang, N. Ren, Monolithic porous Magnéli-phase Ti_4O_7 for electro-oxidation treatment of industrial wastewater, Electrochim. Acta 214 (2016) 326-335. https://doi.org/10.1016/j.electacta.2016.08.037.

[38] K. Yang, L. Hui, S. Liang, R. Xie, S. Lv, J. Niu, C. Jie, Y. Hu, A reactive electrochemical filter system with an excellent penetration flux porous Ti/SnO_2-Sb filter for efficient contaminant removal from water, RSC Adv. 8 (2018) 13933-13944. https://doi.org/10.1039/C8RA00603B.

[39] G.O.H. Whillock, B.F. Harvey, Ultrasonically enhanced corrosion of 304L stainless steel I: The effect of temperature and hydrostatic pressure, Ultrason. Sonochem. 4 (1997) 23-31. https://doi.org/https://doi.org/10.1016/S1350-4177(96)00014-4.

[40] A. Regalado-Méndez, A. Cruz-López, J. Mentado-Morales, M.E. Cordero, L.G. Zárate, M.R. Cruz-Díaz, G. Fontana, E. Peralta-Reyes, Mathematical modeling of the electrochemical degradation of 2-chlorophenol using an electrochemical flow reactor equipped with BDD electrodes, J. Flow Chem. 9 (2019) 59-71. https://doi.org/10.1007/s41981-018-00027-4.

[41] F.F. Rivera, L. Castañeda, P.E. Hidalgo, G. Orozco, Study of hydrodynamics at Asahi™ prototype electrochemical flow reactor, using computational fluid dynamics and experimental characterization techniques, Electrochim. Acta 245 (2017) 107-117. https://doi.org/10.1016/j.electacta.2017.05.134.

[42] J. Teng, G. Liu, J. Liang, S. You, Electrochemical oxidation of sulfadiazine with titanium suboxide mesh anode, Electrochim. Acta 331 (2020) 135441. https://doi.org/10.1016/j.electacta.2019.135441.

[43] S. Levine, A.L. Smith, Theory of the differential capacity of the oxide/aqueous electrolyte interface, Discuss. Faraday Soc. 52 (1971) 290-301. https://doi.org/10.1039/DF9715200290.

[44] J. Chen, L. Guo, X. Hu, Z. Cao, Y. Wang, Dynamics of single bubble departure from TiO_2 nanorod-array photoelectrode, Electrochim. Acta 274 (2018) 57-66. https://doi.org/10.1016/j.electacta.2018.04.051.

[45] G.I. Eskin, Cavitation mechanism of ultrasonic melt degassing, Ultrason. Sonochem. 2 (1995) S137-S141. https://doi.org/10.1016/1350-4177(95)00020-7.

[46] Q. Jin, S.T. Kang, Y.C. Chang, H. Zheng, C.K. Yeh, Inertial cavitation initiated by polytetrafluoroethylene nanoparticles under pulsed ultrasound stimulation, Ultrason. Sonochem. 32 (2016) 1-7. https://doi.org/10.1016/j.ultsonch.2016.02.009.

[47] Y. Bo, J. Zuo, L. Peng, K. Wang, Y. Xin, M. Zhang, Effective ultrasound electrochemical degradation of biological toxicity and refractory cephalosporin pharmaceutical wastewater, Chem. Eng. J. 287 (2016) 30-37. https://doi.org/10.1016/j.cej.2015.11.033.

[48] Y. Huang, T. Zhou, X. Wu, J. Mao, Efficient sonoelectrochemical decomposition of sulfamethoxazole adopting common Pt/graphite electrodes: The mechanism and favorable pathways,

Ultrason. Sonochem. 38 (2017) 735-743. https://doi.org/10.1016/j.ultsonch.2016.08.007.

[49] C. Zhu, C. Jiang, S. Chen, R. Mei, X. Wang, J. Cao, L. Ma, B. Zhou, Q. Wei, G. Ouyang, Z. Yu, K. Zhou, Ultrasound enhanced electrochemical oxidation of Alizarin Red S on boron doped diamond(BDD) anode: Effect of degradation process parameters, Chemosphere 209 (2018) 685-695. https://doi.org/10.1016/j.chemosphere.2018.06.137.

[50] D. Bejan, E. Guinea, N.J. Bunce, On the nature of the hydroxyl radicals produced at boron-doped diamond and Ebonex® anodes, Electrochim. Acta 69 (2012) 275-281. https://doi.org/10.1016/j.electacta.2012.02.097.

[51] F. Parvizian, M. Rahimi, S.M. Hosseini, S.S. Madaeni, A.A. Alsairafi, The effect of high frequency ultrasound on diffusion boundary layer resistance in ion-exchange membrane transport, Desalination 286 (2012) 155-165. https://doi.org/10.1016/j.desal.2011.11.016.

[52] M. Hujjatul Islam, B. Naidji, L. Hallez, A. Et Taouil, J.-Y. Hihn, O.S. Burheim, B.G. Pollet, The use of non-cavitating coupling fluids for intensifying sonoelectrochemical processes, Ultrason. Sonochem. 66 (2020) 105087. https://doi.org/https://doi.org/10.1016/j.ultsonch.2020.105087.

[53] R. Pflieger, T. Chave, G. Vite, L. Jouve, S.I. Nikitenko, Effect of operational conditions on sonoluminescence and kinetics of H_2O_2 formation during the sonolysis of water in the presence of Ar/O_2 gas mixture, Ultrason. Sonochem. 26 (2015) 169-175. https://doi.org/10.1016/j.ultsonch.2015.02.005.

[54] X. Lu, J. Zhao, Q. Wang, D. Wang, H. Xu, J. Ma, W. Qiu, T. Hu, Sonolytic degradation of bisphenol S: Effect of dissolved oxygen and peroxydisulfate, oxidation products and acute toxicity, Water Res. 165 (2019) 114969. https://doi.org/10.1016/j.watres.2019.114969.

[55] M. Panizza, G. Cerisola, Application of diamond electrodes to electrochemical processes,

Electrochim. Acta 51 (2006) 191-199. https://doi.org/10.1016/j.electacta.2005.04.023.

[56] D. Zollinger, U. Griesbach, H. Pütter, C. Comninellis, Electrochemical cleavage of 1,2-diphenylethanes at boron-doped diamond electrodes, Electrochem. Commun. 6 (2004) 605-608. https://doi.org/10.1016/j.elecom.2004.04.014.

[57] C.A. Martinez-Huitle, S. Ferro, A.D. Battisti, Electrochemical incineration of oxalic acid: Role of electrode material, Electrochim. Acta 49 (2004) 4027-4034. https://doi.org/10.1016/j.electacta.2004.01.083.

[58] J. Iniesta, P.A. Michaud, C. Comninellis, Electrochemical oxidation of phenol at boron-doped diamond electrode, Electrochim. Acta 46 (2002) 3573-3578. https://doi.org/10.1016/S0013-4686(01)00630-2.

[59] A. Benyoucef, S. Boussalem, M.I. Ferrahi, M. Belbachir, Electrochemical polymerization and in situ FTIRS study of conducting polymers obtained from o-aminobenzoic with aniline at platinum electrodes, Synth. Met. 160 (2010) 1591-1597. https://doi.org/10.1016/j.synthmet.2010.05.020.

Figure Captions

Fig. 1 Profiles of (a) XRD and (b) XPS, (c) SEM image, (d, e) Hg intrusion porosimetry analysis, and (f) EIS data of TiSO-REM anode.

Fig. 2 Permeate flux under TMP of (a) 0.005 MPa without ultrasound, (b) 0.025 MPa without ultrasound, and (c) 0.025 MPa with ultrasound. Simulated velocity distribution under TMP of 0.025 MPa at (d) 0 V in EO, (e) 3 V in EO, and (f) 3 V in EO-US.

Fig. 3 Reaction rate constants for 4-CP oxidation at anode potential of (a) 1.0 V, (b) 2.0 V and (c) 3.0 V vs SHE. Since k_{US} was determined without external voltage applied and k_{US} curves would be the same in (a), (b) and (c), we only presented the k_{US} curve in (a).

Fig. 4 The current-time curve for TiSO-REM at potential of 2 V vs SHE in (a) EO and (b) EO-US system with injection of 4-CP (10 mg L^{-1}). ESR spectra for TiSO-REM after 30-min electrolysis in (c) ultrasound, (d) EO, and (e) EO-US system at potential of 3 V vs SHE.

Fig. 5 DFT calculations of free energy profiles for (a) $[4\text{-CP}]^{\bullet+}$ oxidation and (b) 4-CP oxidation by electrochemically produced •OH. The inserted figure shows the activation energy as function of electrode potential for DET reaction of 4-CP.

Fig. 6 (a) COD removal tested for 100 cycles, (b) element mass percentage after cyclic test, SEM images of TiSO-REM in (c) EO-US, and (d) EO system. (e-g) FT-IR spectra of the fouling layer formed on TiSO-REM anode.

Fig. 1

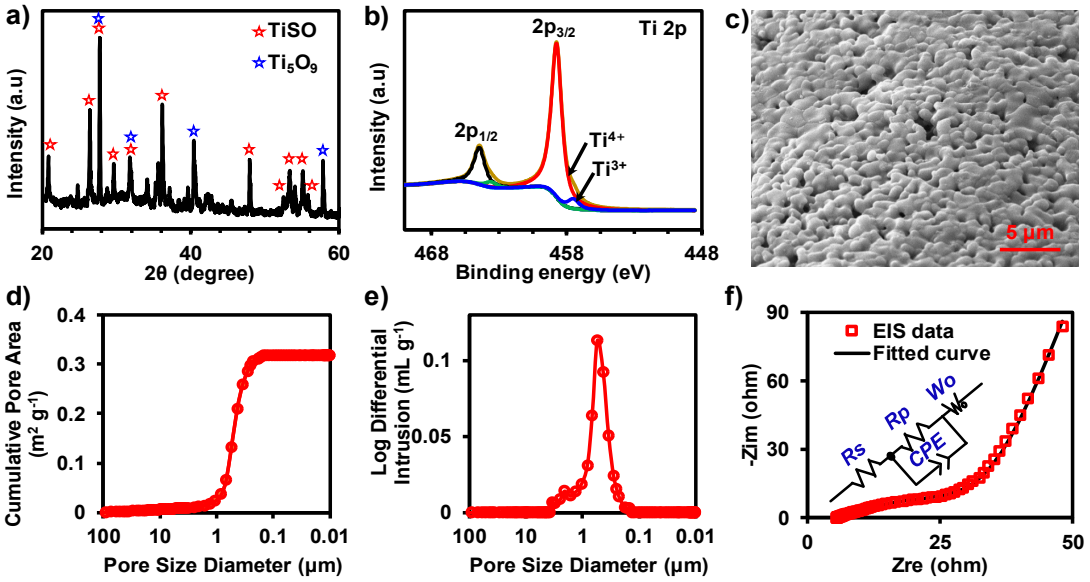
a)
TiSO
Ti5O9
Intensity (a.u)
20
40
60
2θ (degree)
b)
2p3/2
Ti 2p
2p1/2
Ti4+
Ti3+
Intensity (a.u)
468
458
448
Binding energy (eV)
c)
5 µm
d)
Cumulative Pore Area (m2 g-1)
0.4
0.3
0.2
0.1
0
100
10
1
0.1
0.01
Pore Size Diameter (µm)
e)
Log Differential Intrusion (mL g-1)
0.1
0.05
0
100
10
1
0.1
0.01
Pore Size Diameter (µm)
f)
EIS data
Fitted curve
Rs
Rp
Wo
CPE
-Zim (ohm)
90
60
30
0
0
25
50
Zre (ohm)

Fig. 2

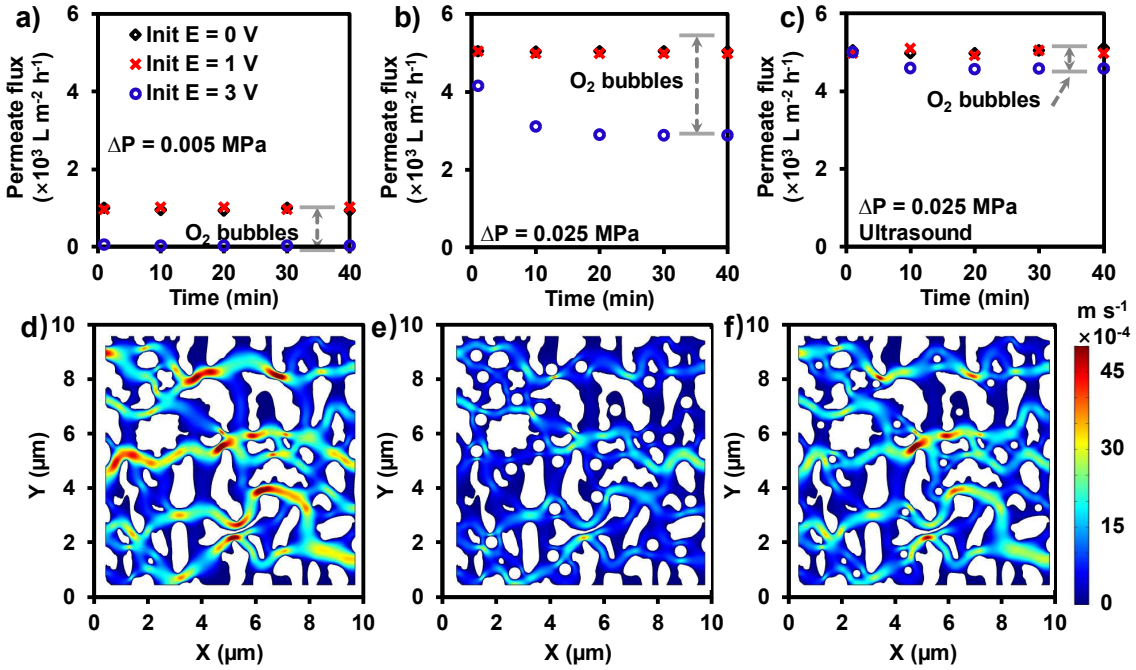
a)
b)
c)
Init E = 0 V
Init E = 1 V
Init E = 3 V
ΔP = 0.005 MPa
ΔP = 0.025 MPa
Ultrasound
O2 bubbles
Permeate flux (×10³ L m⁻² h⁻¹)
Time (min)
d)
e)
f)
Y (μm)
X (μm)
m s⁻¹ ×10⁻⁴
45
30
15
0

Fig. 3

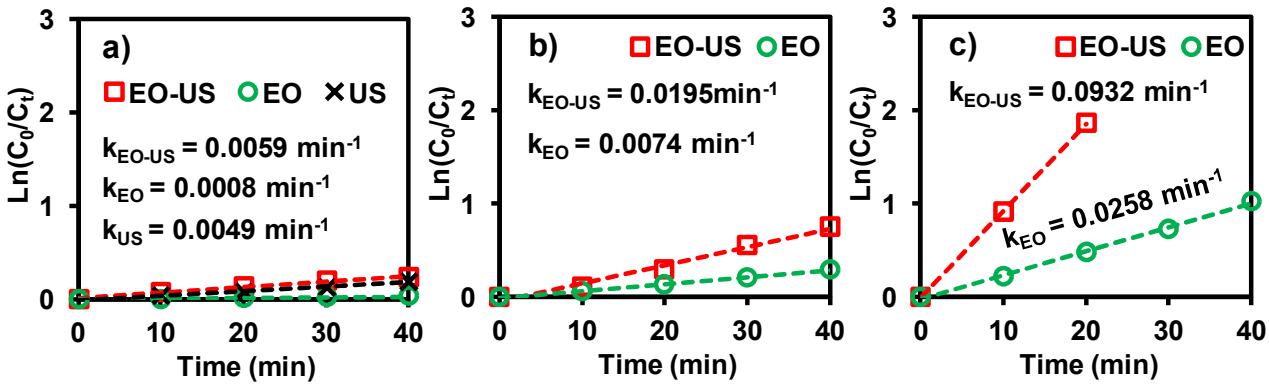
a)
EO-US
EO
US
k_{EO-US} = 0.0059 min^{-1}
k_{EO} = 0.0008 min^{-1}
k_{US} = 0.0049 min^{-1}
b)
EO-US
EO
k_{EO-US} = 0.0195min^{-1}
k_{EO} = 0.0074 min^{-1}
c)
EO-US
EO
k_{EO-US} = 0.0932 min^{-1}
k_{EO} = 0.0258 min^{-1}
$Ln(C_0/C_t)$
Time (min)
0
10
20
30
40
1
2
3

Fig. 4

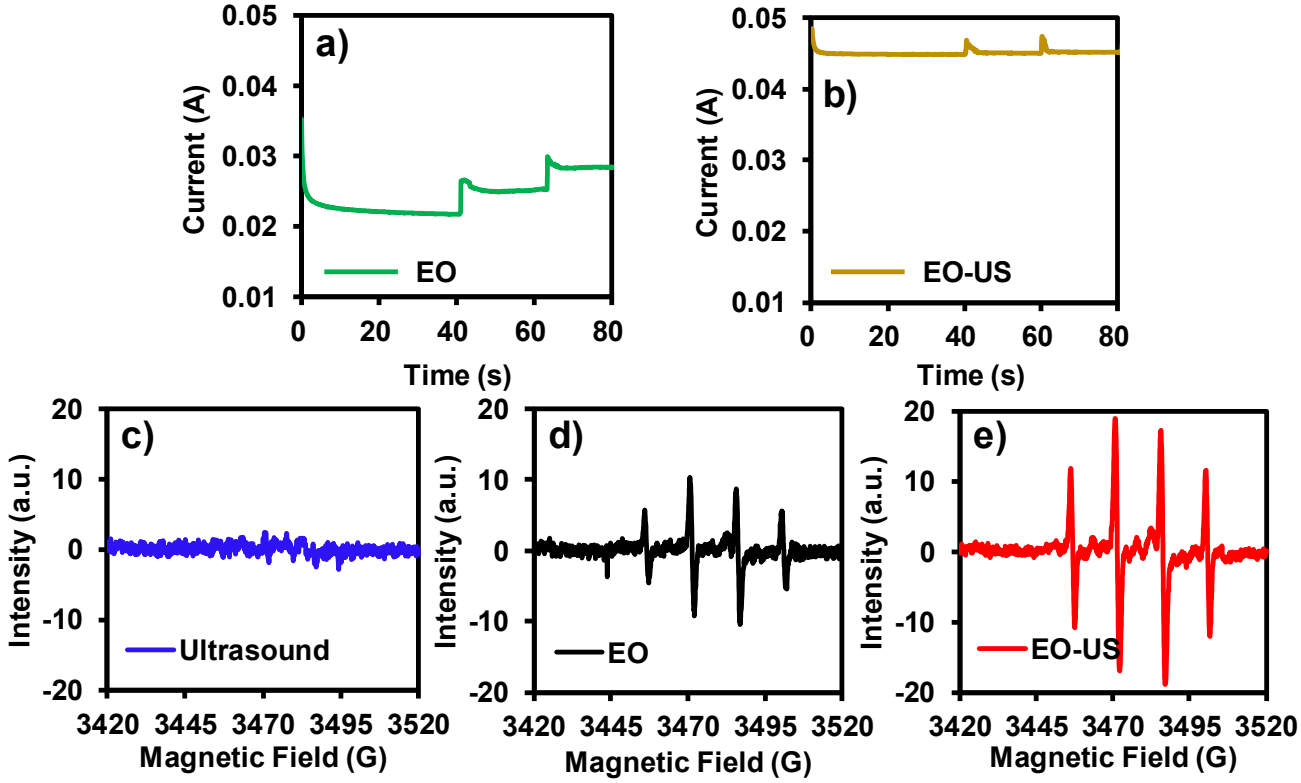
a)
Current (A)
0.05
0.04
0.03
0.02
0.01
EO
0
20
40
60
80
Time (s)
b)
Current (A)
EO-US
Time (s)
c)
Intensity (a.u.)
20
10
0
-10
-20
Ultrasound
3420 3445 3470 3495 3520
Magnetic Field (G)
d)
EO
e)
EO-US

Fig. 5

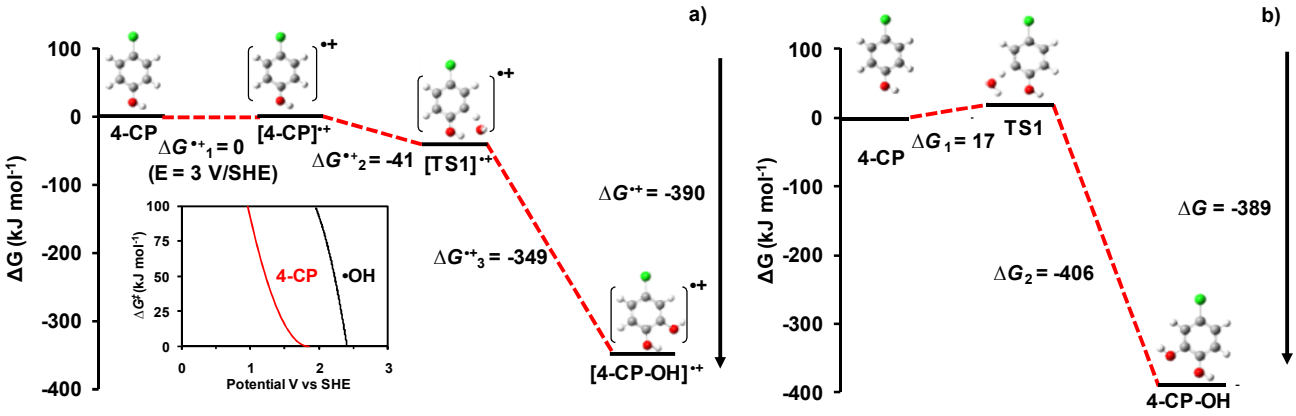
a)
b)
ΔG (kJ mol-1)
100
0
-100
-200
-300
-400
4-CP
[4-CP]•+
[TS1]•+
[4-CP-OH]•+
ΔG•+1 = 0
(E = 3 V/SHE)
ΔG•+2 = -41
ΔG•+3 = -349
ΔG•+ = -390
4-CP
•OH
ΔGf (kJ mol-1)
Potential V vs SHE
ΔG1 = 17
TS1
ΔG2 = -406
ΔG = -389
4-CP-OH

Fig. 6

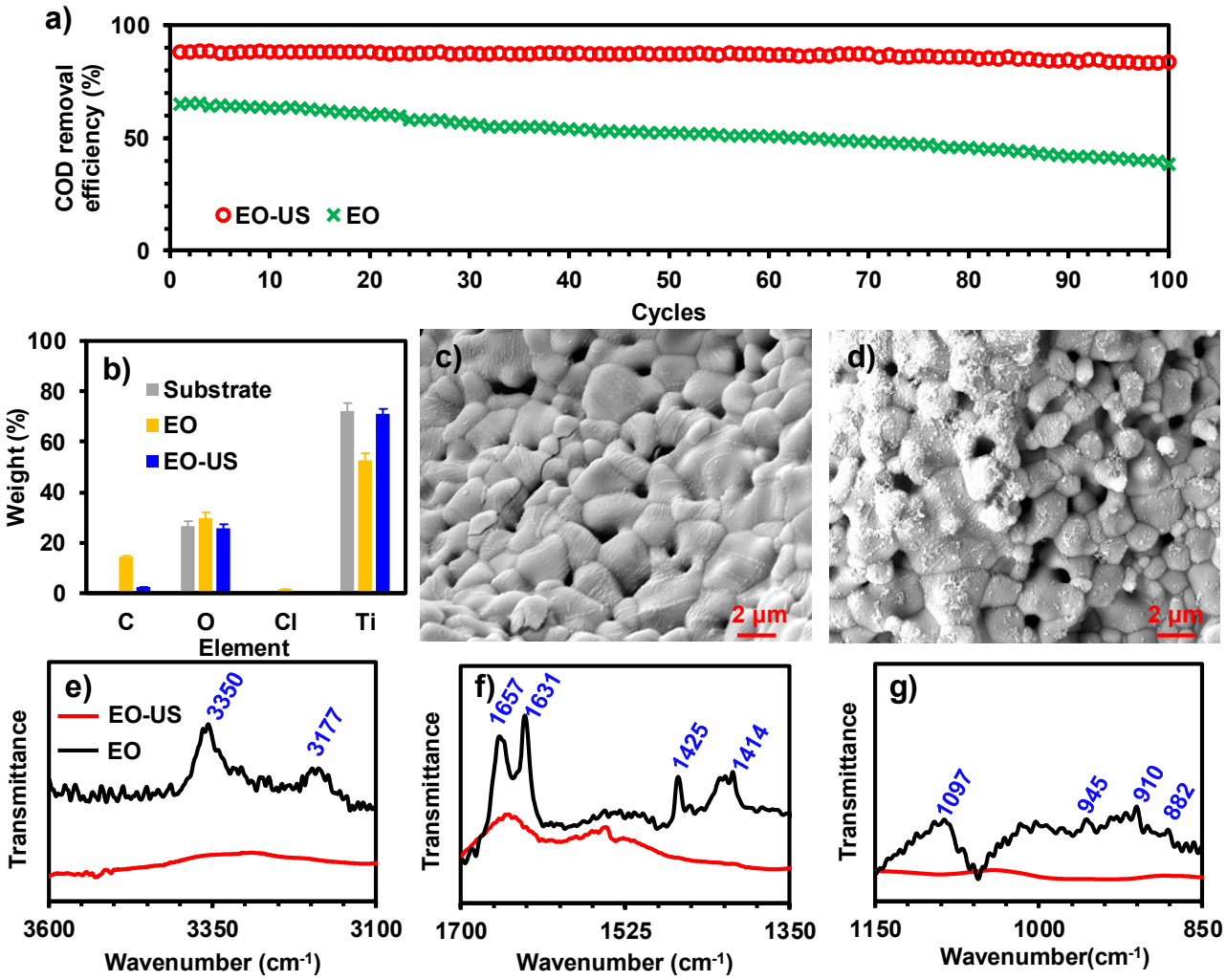
a)
COD removal efficiency (%)
EO-US
EO
Cycles
b)
Substrate
EO
EO-US
Weight (%)
C
O
Cl
Ti
Element
c)
2 μm
d)
2 μm
e)
EO-US
EO
3350
3177
Transmittance
Wavenumber (cm-1)
f)
1657
1631
1425
1414
Transmittance
Wavenumber (cm-1)
g)
1097
945
910
882
Transmittance
Wavenumber(cm-1)